Electronic Supplementary Material (ESI) for Journal of Materials Chemistry A.
This journal is © The Royal Society of Chemistry 2024

Electronic Supporting Information (ESI)

A conjugated microporous polymer–graphene composite porous sandwich-like film for highly efficient flexible supercapacitors

Likuan Teng, Ju Duan, He Liu, Xinzeyu Zhang, Jiaqiang Li, Yitao Li, Jianhao Hong, Wei Lyu*, Yaozu Liao*

State Key Laboratory for Modification of Chemical Fibers and Polymer Materials, College of Materials Science and Engineering, Donghua University, Shanghai 201620, China.

*Corresponding author. E-mail: wlyu@dhu.edu.cn; yzliao@dhu.edu.cn

Table of contents

S1. Materials

Tris(4-bromophenyl)amine (TBA, > 98%), 2-Dicyclohexylphosphino-2′,4′,6′-triisopropylbiphenyl (XPhos, > 98%) and bis (dibenzylideneacetone) palladium (0) (Pd(dba)2, > 99%) were purchased from Tokyo Chemical Industry (TCI) Development Co., Ltd. 4-Aminobenzene-1,2-diol hydrobromide (ABDH, 97%) was purchased from Bidepharm. *p*-Phenylenediamine (*p*-PDA, > 99%), sodium tert-butoxide (NaOtBu, > 99%), Polyvinyl alcohol 124 (PVDF 124) and sulfuric acid (H_2SO_4, 95%) were purchased from Sinopharm Chemical Reagent Co., Ltd. Tetrahydrofuran (THF, > 99%), chloroform (> 99%), methanol (> 99.5%), Ethanol (> 99.5%), Hydroiodic acid (RG, 55-57 wt% aqueous solution) were purchased from Shanghai Titan Scientific Co., Ltd. Sodium fluoride (NaF, > 99%) was purchased from Shanghai Macklin Biochemical Co. Ltd. Flake graphite (800 mesh) was purchased from Guangdong Canrd New Energy Technology Co., Ltd.

S2. Materials characterization

Fourier transform infrared spectra (FT-IR) were performed on a Nicolet 670 spectrometer. Raman spectra were taken on an Renishaw inVia-Reflex apparatus. An excitation wavelength of 633 nm was used. Brunauer-Emmett-Teller (BET) model were used to calculate the specific surface areas using the adsorption branches of the N_2 isotherms by using the Micro for ASAP2460 software package at 77 K after degassing samples under high vacuum at 120 ℃ for 15 h. The pore size distribution was calculated from the desorption branch of the N_2 isotherms using the nonlocal density functional theory (NLDFT). Scanning electron microscope (SEM) images were obtained on a HITACHI *Regulus8230 SEM and transmission electron microscope (TEM) images were obtained on a Talos F200S TEM. The powder-like samples for SEM and TEM studies were prepared by dispersing into EtOH solution under ultrasonic irradiation. Thermal gravimetric analysis (TGA) was measured on a Libra/209F1 instrument under N_2 atmosphere in the temperature ranging from 30 to 900 ℃, with heating rate of 10 ℃ min^{-1}. X-ray photoelectron spectra (XPS) were performed on an Escalab 250Xi spectrometer. Solid-state cross-polarization magic angle spinning ^{13}carbon nuclear magnetic resonance (^{13}C CP/MAS NMR) spectra of all samples was

recorded on an AVANCE400 instrument. The crystallinity of the samples was characterized by a Bruker D8 ADVANCE X-ray diffraction (XRD) spectrometer. Dynamic light scattering (DLS) was tested on the NANO ZS instrument. The electrical conductivity of composite film was measured at room temperature via a four-point probe instrument (Loresta-AX MCP-T370, Mitsubishi Chemical Analytech Co., Ltd). At least three locations on the films were measured for each sample to determine the average electrical conductivity.

S3. Electrochemical characterization

S3.1. Electrochemical characterization of individual films electrode

Electrochemical measurements including, cyclic voltammetry (CV), galvanostatic charge-discharge (GCD) and electrochemical impedance spectroscopy (EIS) were performed on a Gamry Interface1100E electrochemical workstation at room temperature in 1 M H_2SO_4 aqueous solution with a three-electrode system, using individual film electrode, Pt wire and Ag/AgCl (3M KCl) as the working electrode, counter electrode and reference electrode, respectively. The EIS was investigated in the frequency ranging from 10^6 Hz to 0.1 Hz with an open circuit voltage amplitude of 5 mV.

C_{three}(F g^{-1}) was calculated from the GCD by the presented equation (1):

$$C_{three} = \frac{\mathrm{I}}{\mathrm{mdV/dt}} \tag{1}$$

where I(A) is the discharge current, m(g) is the mass of film electrode and $dV/dt=(V_{max}-1/2V_{max})/(t_2-t_1)$, t_1 and t_2 (s) are the discharge times at the points of maximum potential (V_{max} ,V) and half of the voltage ($1/2V_{max}$,V), respectively.[1,2]

S3.2. Electrochemical characterization of the symmetrical supercapacitors (SSCs) and flexible solid-state symmetrical supercapacitors (FSSCs)

The EIS, CV, GCD were also performed on the Gamry Interface1100E electrochemical workstation at room temperature in 0.5 M H_2SO_4 aqueous solution with a symmetric-electrode test cell using two individual films. And the assembled ASSCs was tested directly through the two-electrode system.

C_{two}(F g^{-1}) calculated from the GCD by the presented equation (2):

$$C_{two} = \frac{2I}{MdV/dt} \tag{2}$$

Where C_{two} is the specific capacitance measured in a symmetric two-electrode configuration, M(g)is the total mass of the both electrodes (i.e. $M = M_+ + M_-$).[1]

And C_{FSSC}(F g^{-1}) was calculated from the GCD by the presented equation (3):

$$C_{FSSC} = \frac{2I}{MdV/dt} \tag{3}$$

The areal and volumetric capacitances were calculated by the equations (4) and (5), respectively:

$$C_A = \frac{C_G * m}{A} \tag{4}$$

$$C_V = \frac{C_A * A}{V} = \frac{C_A * 10}{d} \tag{5}$$

Where C_G(F g^{-1}) is the specific capacitance, C_A(mF cm^{-2}) is the areal capacitance, C_V(F cm^{-3}) is the volumetric capacitance, m(g)is the total mass of electrodes, A(cm^2) is the total area of electrodes, d(μm) is the thickness of electrodes.[1] The gravimetric, areal, volumetric capacitances for all samples are listed in Table S7.

The energy density E(W h kg^{-1}) and the power density P(W kg^{-1}) of the SSCs and FSSCs in the Ragone plot were calculated using the following equations:[3]

$$E = \frac{C_{two} \times V^2}{2 \times 4 \times 3.6} \text{ or } E = \frac{C_{ASSC} \times V^2}{2 \times 4 \times 3.6} \tag{6}$$

$$P = \frac{E \times 3600}{\Delta t} \tag{7}$$

S3.3. Electrode kinetics

The degree of capacitive effective for were calculated using Duun's and Trasatti's method is according to the following equations:

$$i = av^b \tag{8}$$

$$\log i = b\log v + \log a \tag{9}$$

where i is the current density, v is the scan rate, and a and b are the variable parameters.

The capacitive contribution ratio under different scan rates was calculated using the following equations:

$$i(V) = k_1 v + k_2 v^{1/2} \tag{10}$$

$$i(V)/v^{1/2} = k_1 v^{1/2} + k_2 v \tag{11}$$

where k_1 or k_2 is a constant for a given potential V.[4,5]

S3.4. Electrochemical characterization of the micro supercapacitors (MSCs)

$C_{MSC,A}$(mF cm^{-2}) calculated from the GCD by the following equation (12):

$$C_{MSC,A} = \frac{\mathrm{I}}{\mathrm{AdV/dt}} \tag{12}$$

Where $C_{MSC,A}$ is the area capacitance of the entire MSCs, A(cm^{-2}) is the total area of the MSC.

The energy density $E_{MSC,A}$(μ Wh cm^{-2}) and the power density $P_{MSC,A}$(m W cm^{-2}) of the entire MSCs were calculated using the following equations:[6]

$$E_{MSC,A} = \frac{C_{MSC,A} \times \mathrm{V}^2}{2 \times 3.6} \tag{13}$$

$$P_{MSC,A} = \frac{E \times 3.6}{\Delta \mathrm{t}} \tag{14}$$

S4. Supplementary Figures and Tables

S4.1. Figures

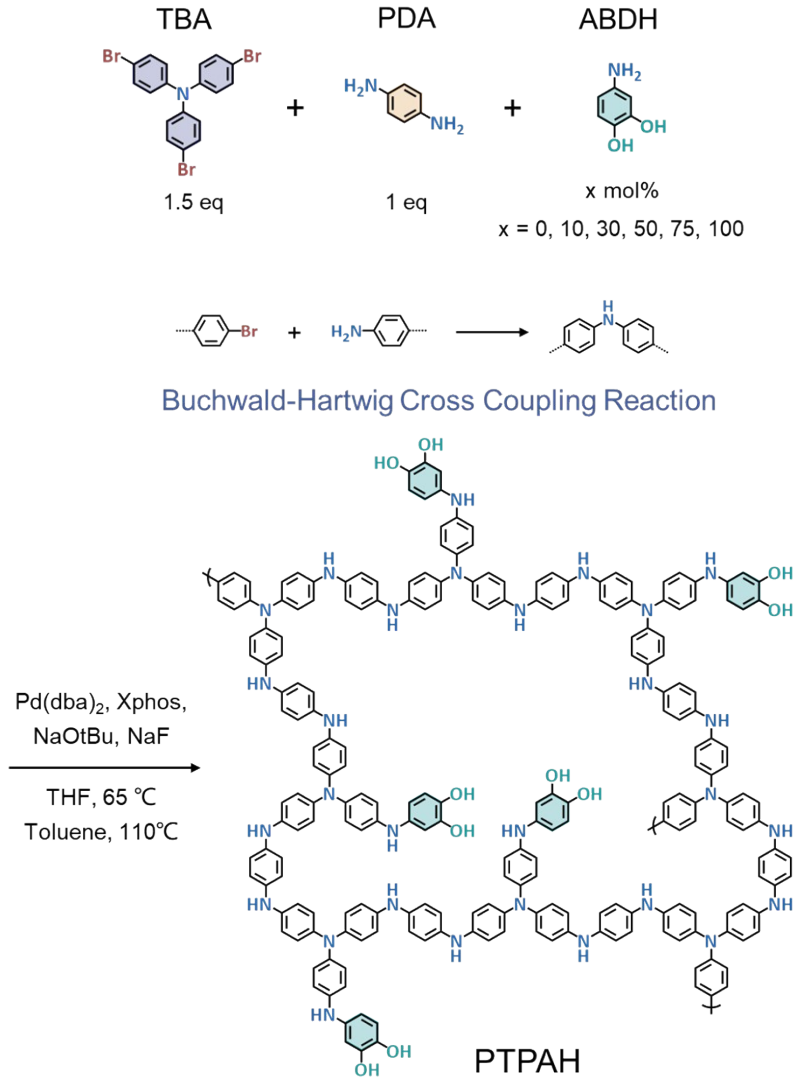

Fig. S1. The synthesis process and reaction mechanisms of PTPAH through Buchwald Hartwig (B-H) cross coupling reaction.

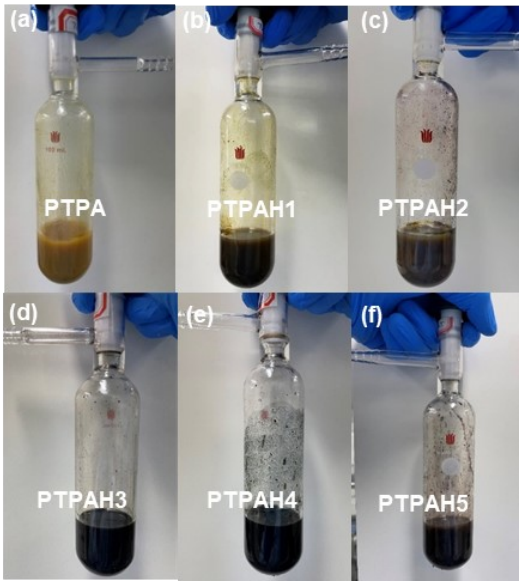

Fig. S2. Photo images of B-H reaction with different ratios of addition of the ABDH. (a) PTPA, (b) PTPAH1, (c) PTPAH2, (d) PTPAH3, (e) PTPAH4, (f) PTPAH5.

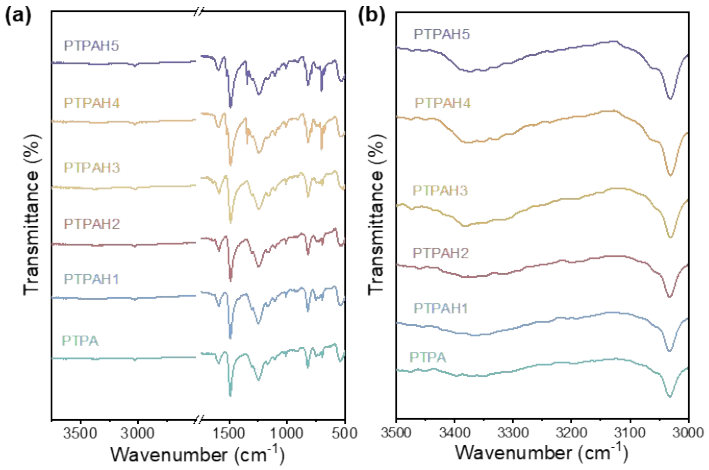

Fig. S3. FT-IR spectra of PTPA and PTPAHs over (a) wavenumber range: 3800-500 cm^{-1}, (b) wavenumber range: 3500-3000 cm^{-1}.

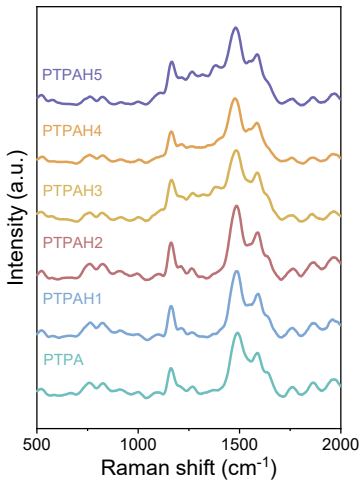

Fig. S4. Raman spectra of PTPA and PTPAHs.

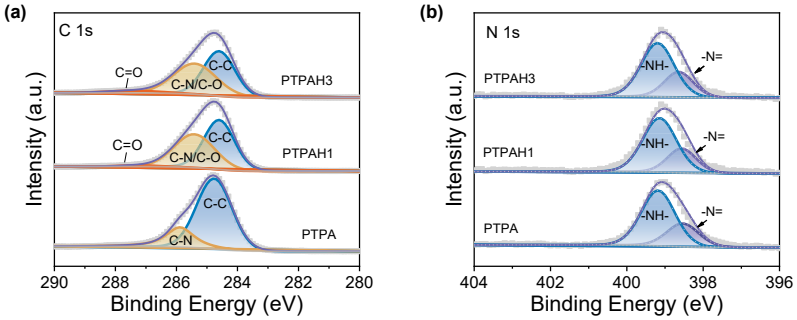

Fig. S5. (a) C1s XPS spectra and (b) N1s XPS spectra of PTPA, PTPAH1 and PTPAH3.

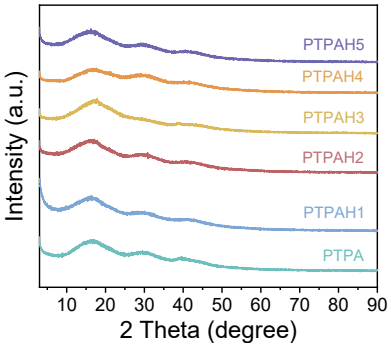

Fig. S6. XRD patterns for PTPA and PTPAHs.

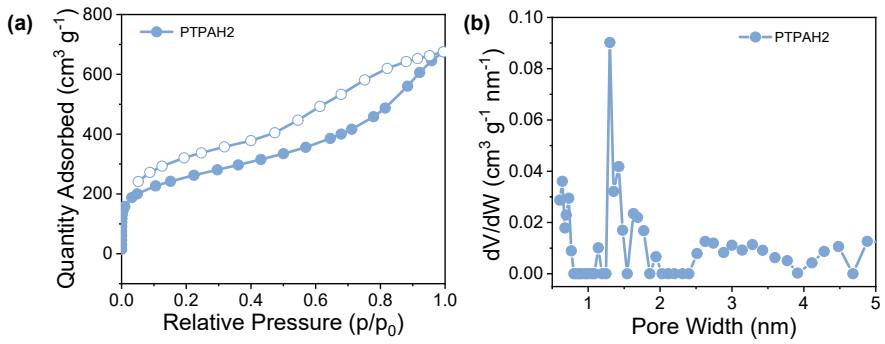

Fig. S7. (a) N_2 adsorption/desorption isotherms (77 K) and (b) pore size distributions using NLDFT model of PTPAH2.

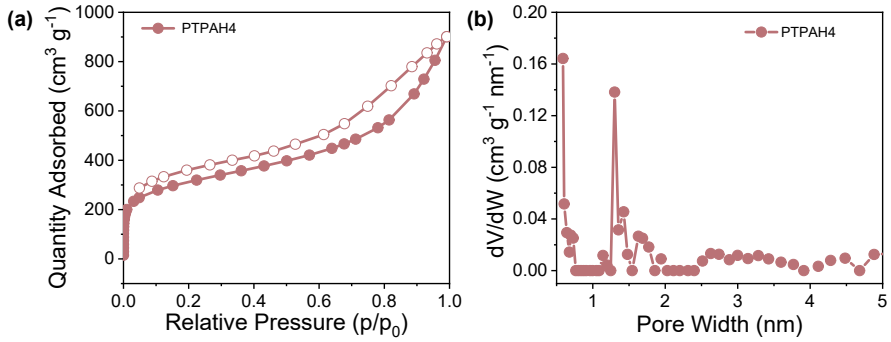

Fig. S8. (a) N_2 adsorption/desorption isotherms (77 K) and (b) pore size distributions using NLDFT model of PTPAH4.

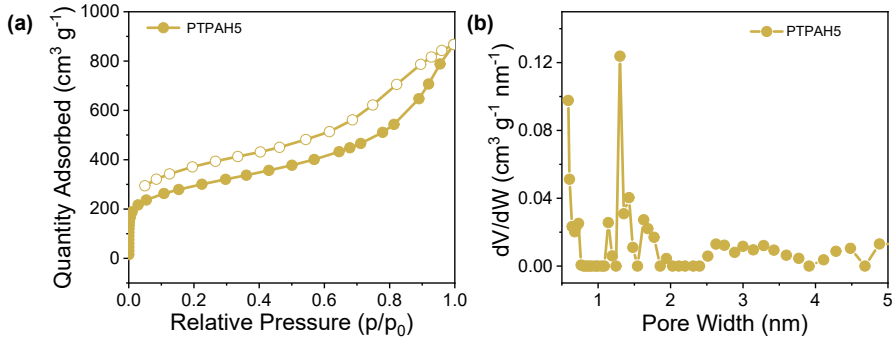

Fig. S9. (a) N_2 adsorption/desorption isotherms (77 K) and (b) pore size distributions using NLDFT model of PTPAH5.

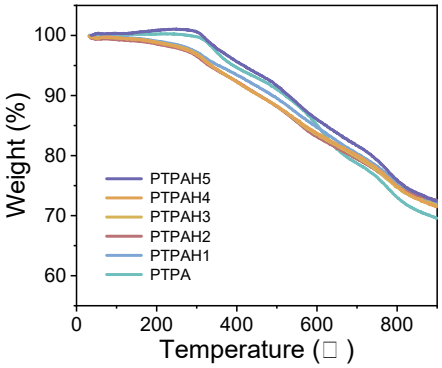

Fig. S10. TGA measurements of PTPA and PTPAHs were carried out in nitrogen atmosphere.

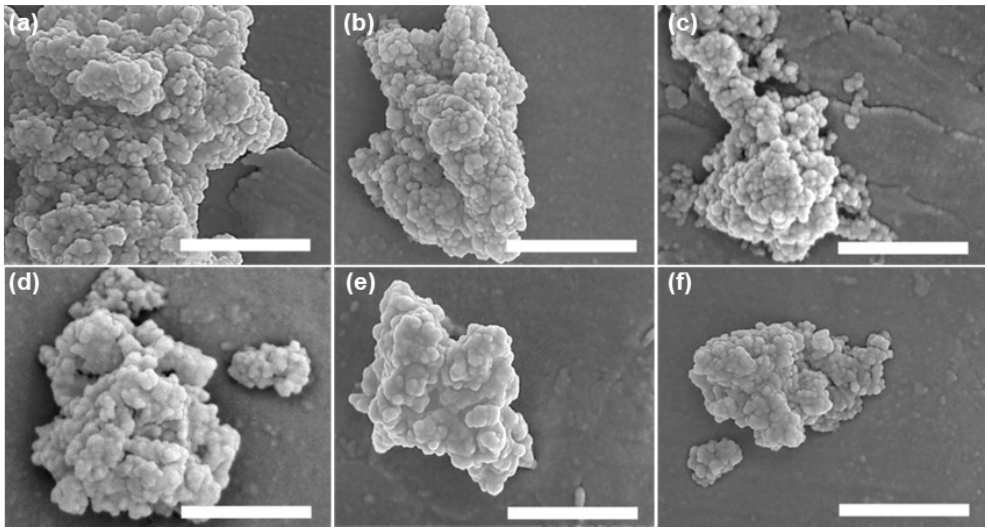

Fig S11. SEM images of (a) PTPA, (b) PTPAH1, (c) PTPAH2, (d) PTPAH3, (e) PTPAH4, (f) PTPAH5. Scale bar: 500 nm.

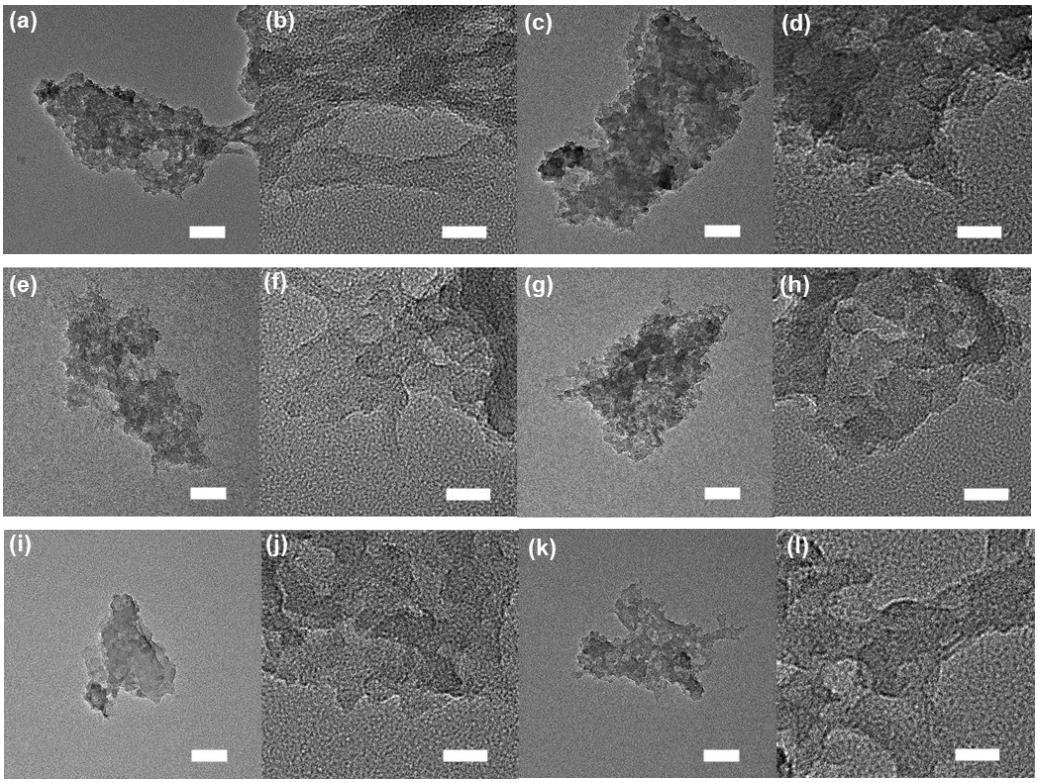

Fig. S12. TEM images of PTPA and PTPAHs (a-b) PTPA, (c-d) PTPAH1, (e-f) PTPAH2, (g-h) PTPAH3, (i-j) PTPAH4, (k-l) PTPAH5. Scale bar: (a, c, e, g, i, k) 100 nm and (b, d, f, h, j, l) 20 nm.

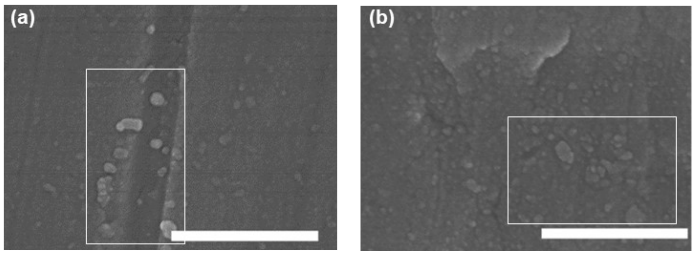

Fig. S13. (a-b) SEM images of well-dispersed particles of PTPAH3. Sacle bar: 500 nm.

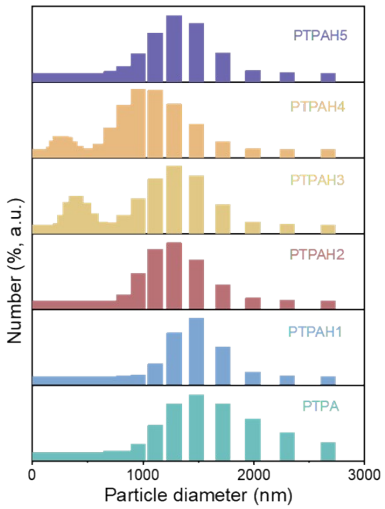

Fig. S14. Size distribution of PTPA and PTPAHs dispersed in aqueous solutions with a concentration of 0.5 mg ml^{-1}

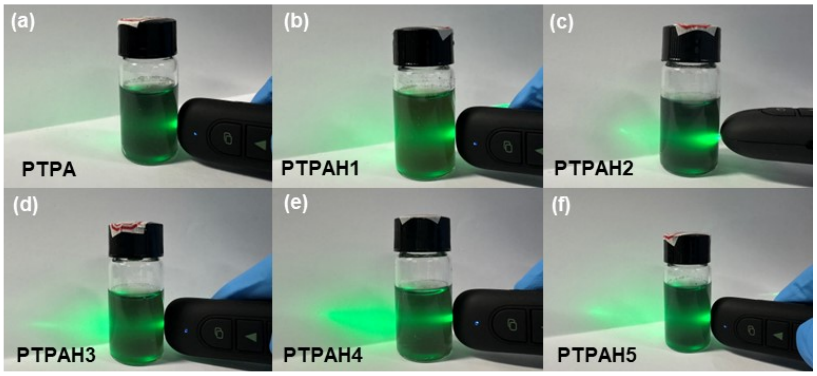

Fig. S15. Photos images of PTPA and PTPAHs dispersed in aqueous solutions under laser irradiation, showing the Tyndall effect and transmitted light. (a) PTPA, (b) PTPAH1, (c) PTPAH2, (d) PTPAH3, (e) PTPAH4, (f) PTPAH5. (i.e. as shown in d and e, the Tyndall effect is obvious and the transmitted intensity is the highest.)

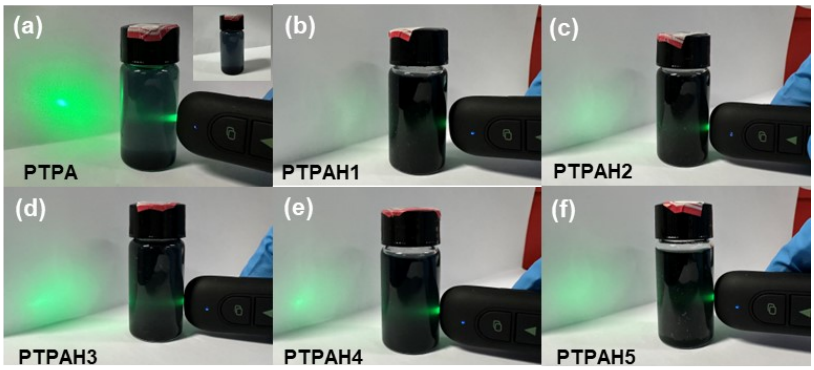

Fig. S16. Photos images of PTPA and PTPAHs dispersed in THF under natural light and laser irradiation, showing the Tyndall effect and transmitted light. (a) PTPA, (b) PTPAH1, (c) PTPAH2, (d) PTPAH3, (e) PTPAH4, (f) PTPAH5. (i.e. as shown in a, PTPA can not be dispersed in THF, there is a lot of settlement at the bottom of the bottle; as shown in d and e, the Tyndall effect is obvious and the transmitted intensity is the highest.)

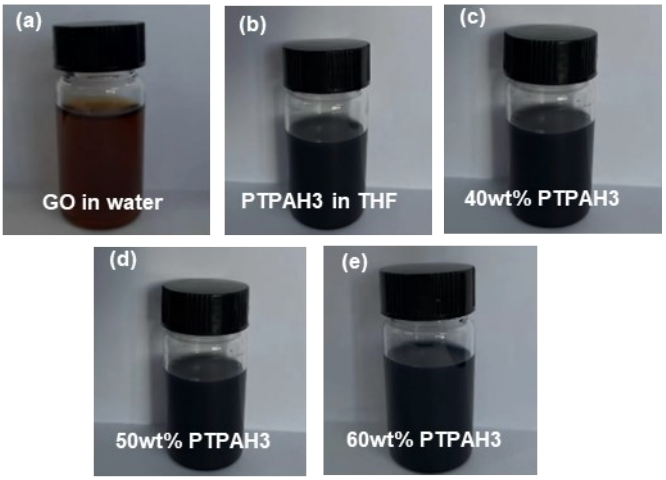

Fig. S17. Photo images of different dispersions (a) GO dispersion in water, (b) PTPAH3 dispersion in THF, (c-e) composites of PTPAH3 and GO dispersion in water/THF under different mass ratios (c) 4/6, w/w, (d) 5/5, w/w, (e) 6/4, w/w.

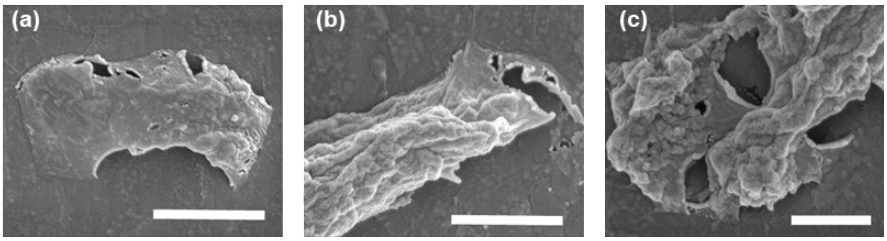

Fig. S18. (a-c) SEM images of PTPAH3@GO under 5/5, w/w. Scale bar: (a-b) 1μm and (c) 500 nm.

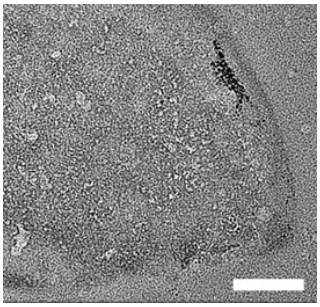

Fig. S19. TEM images of PTPAH3@GO under 5/5, w/w. Scale bar: 100 nm.

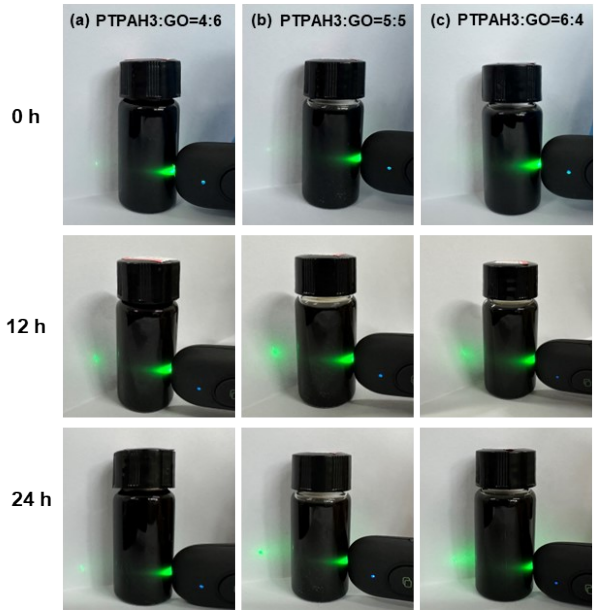

Fig. S20. Photo images of mixed PTPAH3 and GO dispersion in water/THF under laser irradiation after different standing times (0, 12 and 24 h) with different mass ratios (a) 4/6; (b) 5/5 and (c) 6/4, w/w.

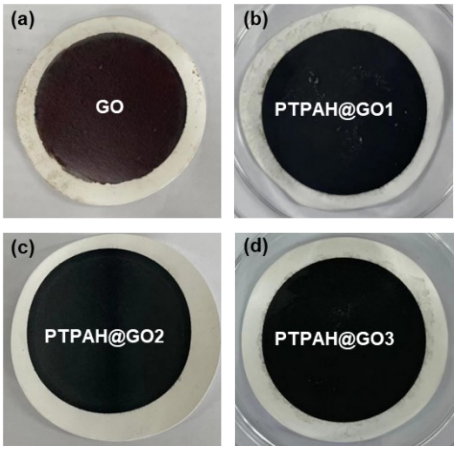

Fig. S21. Photo images of (a) GO film, (b) PTPAH@GO1 film, (c) PTPAH@GO2 film, (d) PTPAH@GO3 film.

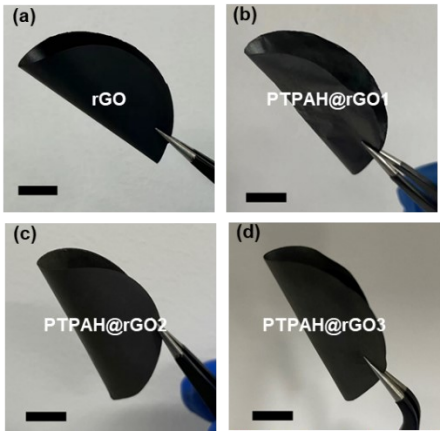

Fig. S22. Photo images of the folded as-prepared film (a) rGO film, (b) PTPAH@rGO1 film, (c) PTPAH@rGO2 film, (d) PTPAH@rGO3 film.

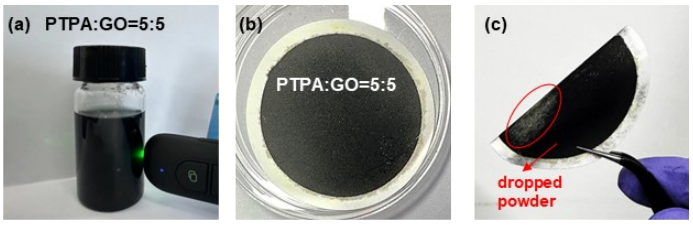

Fig. S23. Photo images of (a) mixed dispersions of PTPA and GO in water/THF under a mass ratio of 5/5, w/w under laser irradiation, (b) the formed PTPA@GO film via vacuum filtration and (c) the folded PTPA@GO film, with circle and arrow indicating the easily dropped off powders.

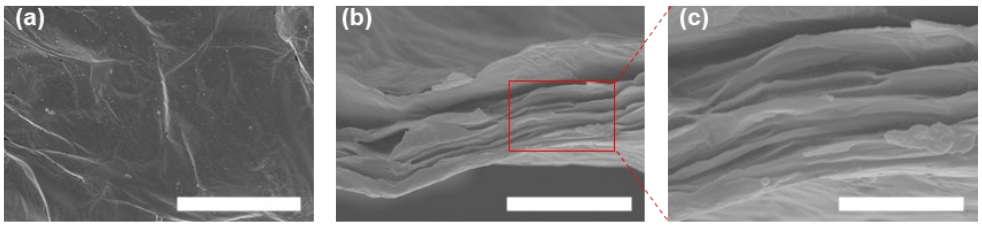

Fig. S24. (a) Top-view and (b-c) side-view SEM images of rGO film. Scale bar: (a) 10 μm, (b) 5 μm, (c) 2 μm.

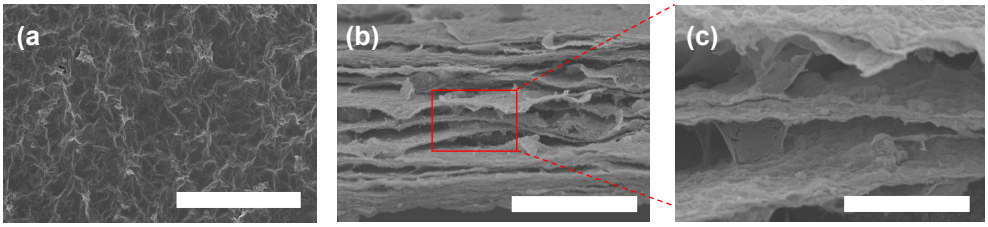

Fig. S25. (a) Top-view and (b-c) side-view SEM images of PTPAH@rGO1 film. Scale bar: (a) 10 μm, (b) 10 μm, (c) 2 μm.

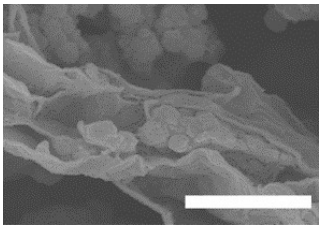

Fig. S26. Side-view SEM images of PTPAH@rGO2 film. Scale bar: 2 μm.

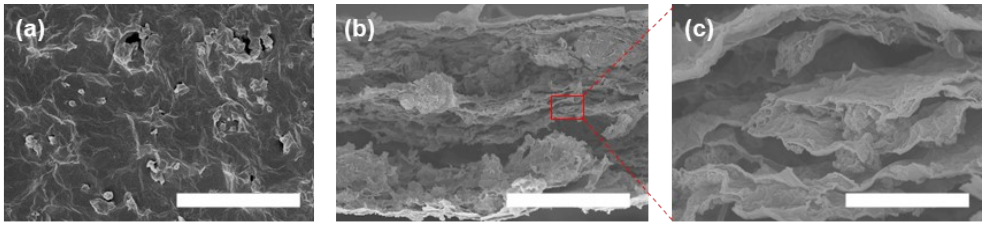

Fig. S27. (a) Top-view and (b-c) side-view SEM images of PTPAH@rGO3 film. Scale bar: (a) 10 μm, (b) 20 μm, (c) 2 μm.

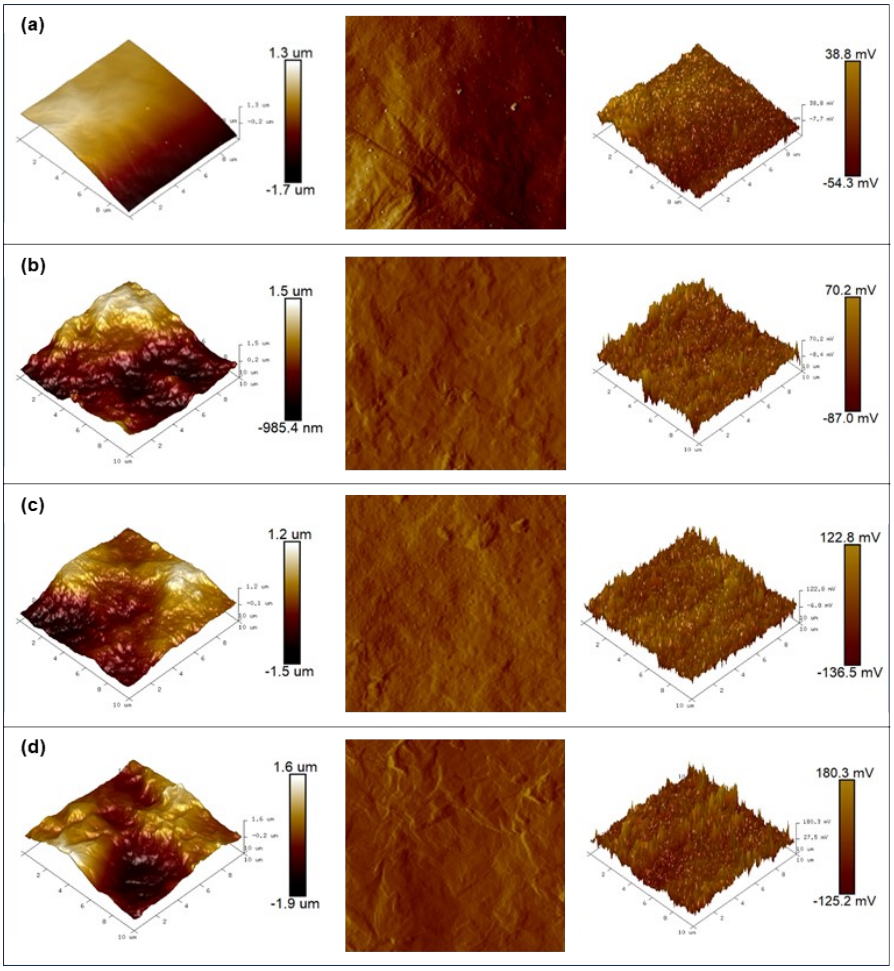

Fig. S28. Atomic force microscope (AFM) images of (a) rGO film, (b) PTPAH@rGO1 film, (c) PTPAH@rGO2 film, (d) PTPAH@rGO3 film.

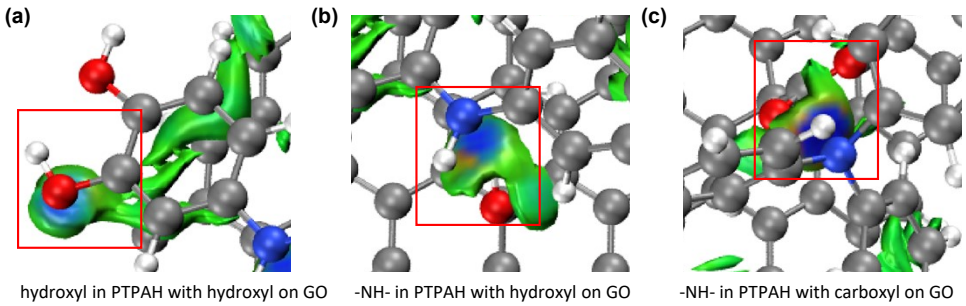

Fig. S29. The intermolecular forces between (a) hydroxyl -OH in PTPAH and hydroxyl -OH on GO, (b) -NH- in PTPAH and hydroxyl -OH on GO, (c) -NH- in PTPAH and carboxyl -OH on GO .

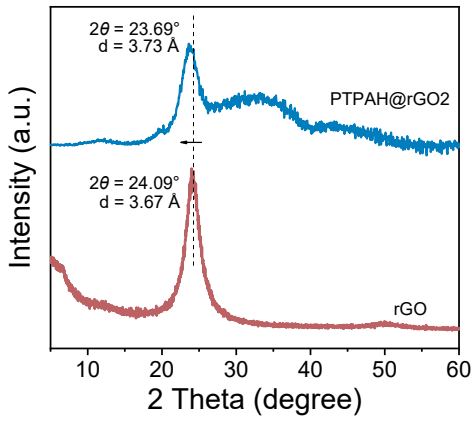

Fig. S30. XRD patterns for rGO and PTPAH@rGO2 film.

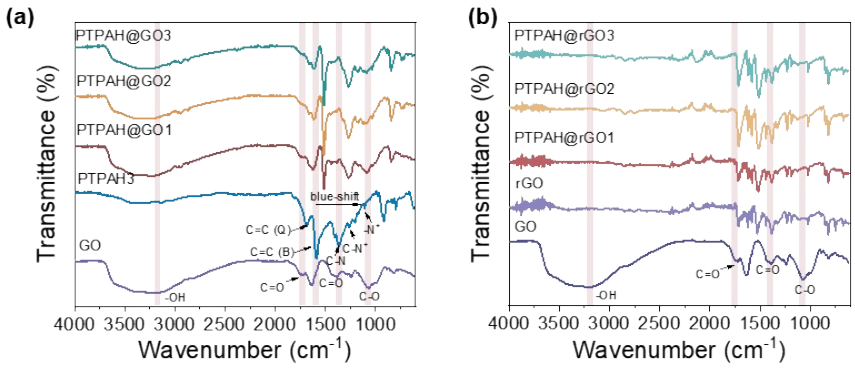

Fig. S31. FTIR spectra of (a)PTPAH3, GO film and PTPAH@GO1-3 films, (b) GO, rGO films and PTPAH@rGO films.

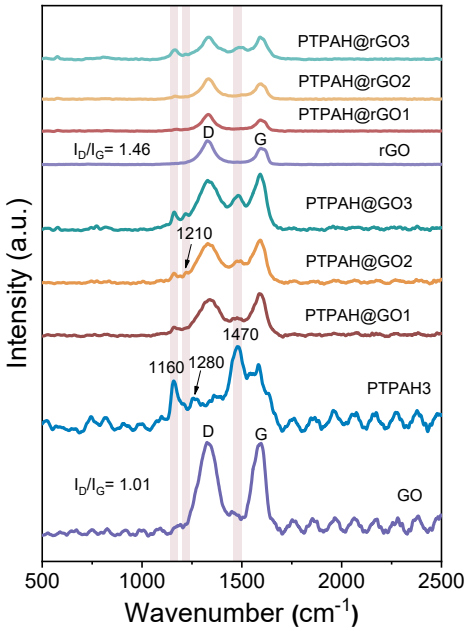

Fig. S32. Raman spectra of PTPAH3, GO film, rGO film and the other composite films. (i.e. Compared with the Raman spectra of each films, with the improving of the mass ratio of PTPAH3, the peaks at 1160 cm^{-1} and 1470 cm^{-1} can be observed and gradually increased.)

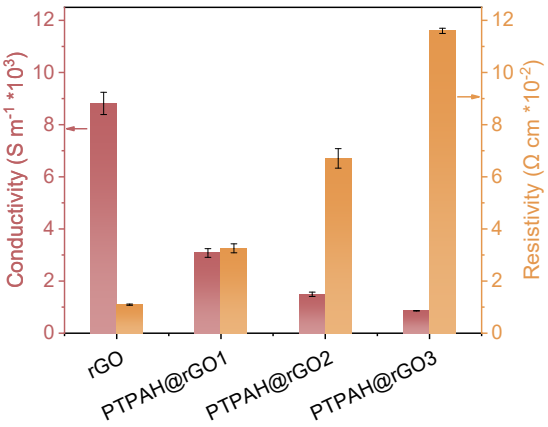

Fig. S33. The resistivity and conductivity of rGO and PTPAH@rGO films measured through four-probe method.

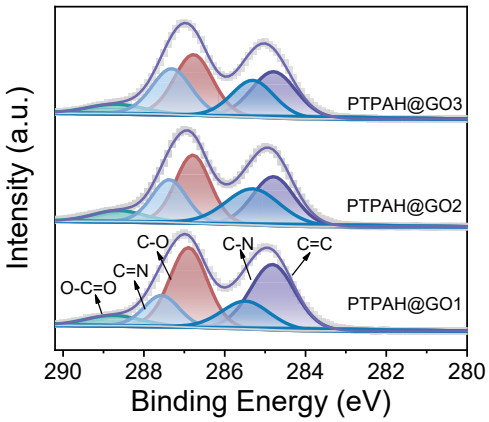

Fig. S34. C 1s XPS spectra of three samples of PTPAH@GOs films.

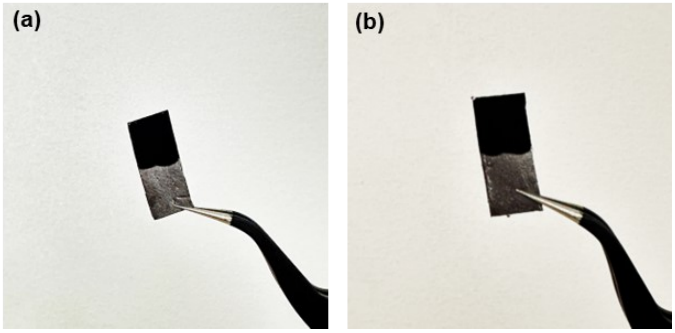

Fig. S35. Photo images of PTPA and PTPAH3 electrodes.

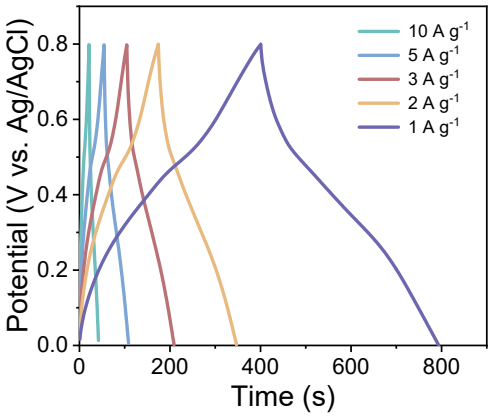

Fig. S36. GCD curves of PTPAH3 in a three-electrode system.

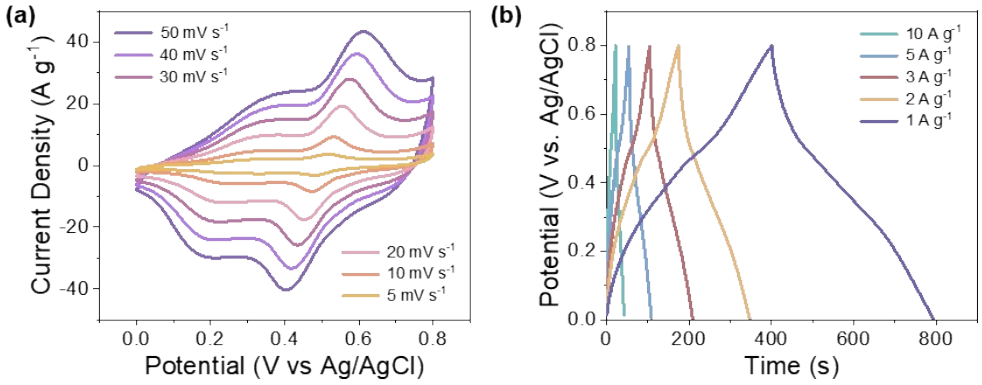

Fig. S37. (a) CV and (b) GCD curves of PTPA in a three-electrode system.

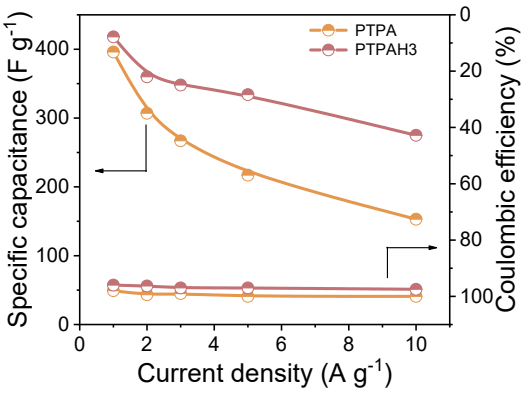

Fig. S38. Specific capacitance and Coulombic efficiency of PTPA and PTPAH3.

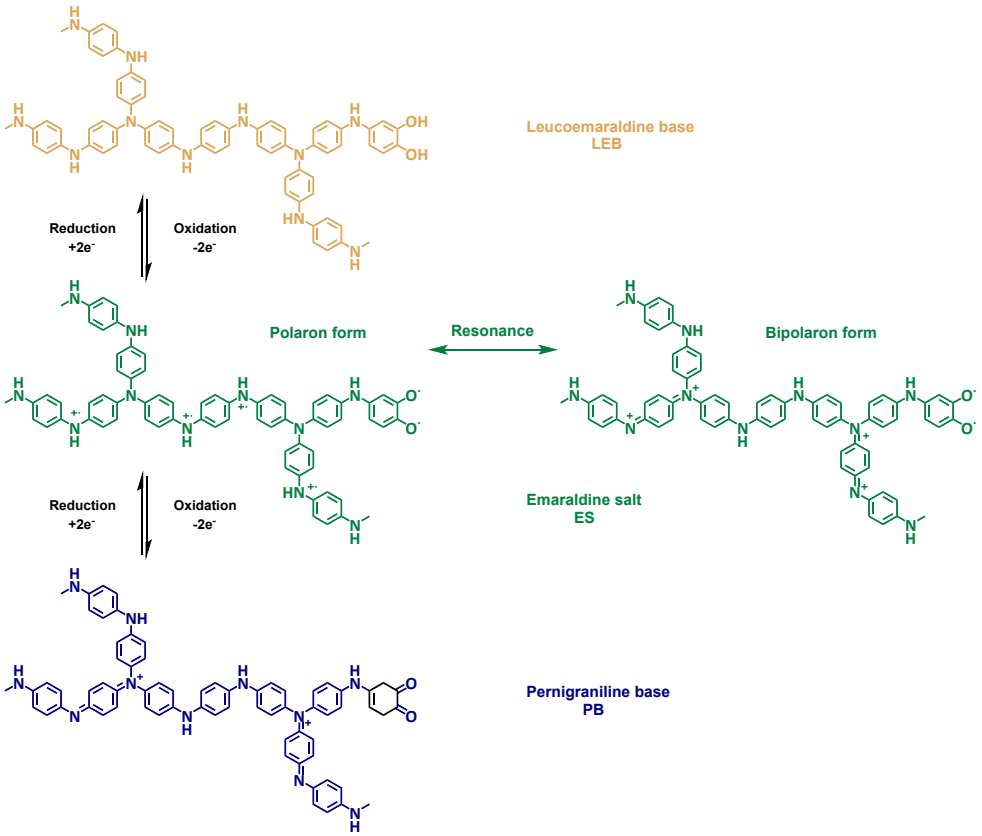

Fig. S39. Proposed redox reactions, i.e., charge and discharge mechanism of PTPAH3.

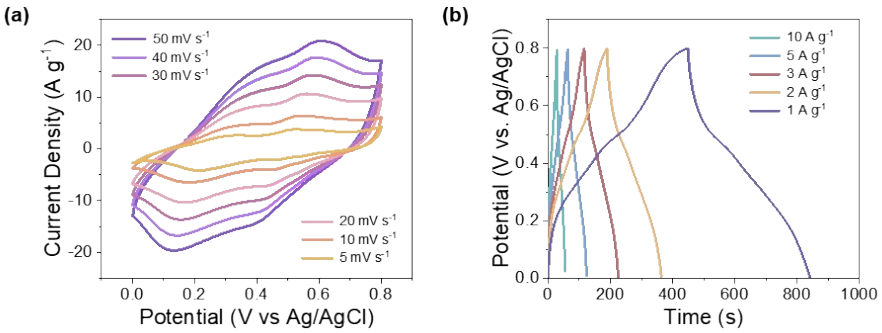

Fig. S40. (a) CV and (b) GCD curves of PTPAH@rGO1 film in a three-electrode system.

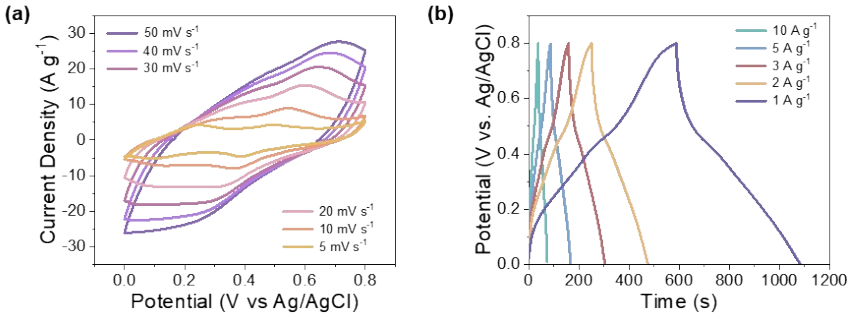

Fig. S41. (a) CV and (b) GCD curves of PTPAH@rGO2 film in a three-electrode system.

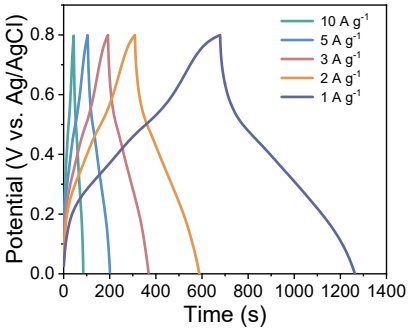

Fig. S42. GCD curves of PTPAH@rGO3 film in a three-electrode system.

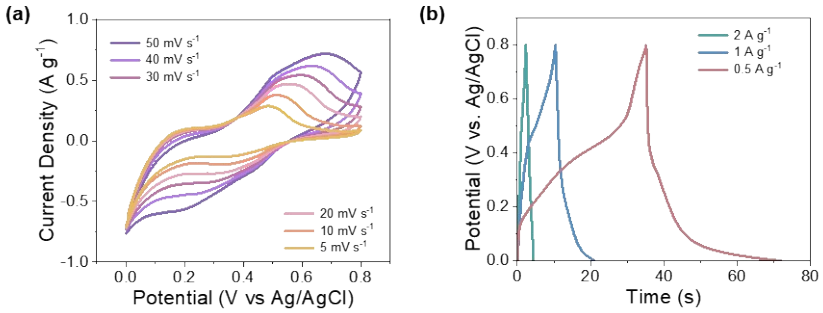

Fig. S43. (a) CV and (b) GCD curves of rGO film in a three-electrode system.

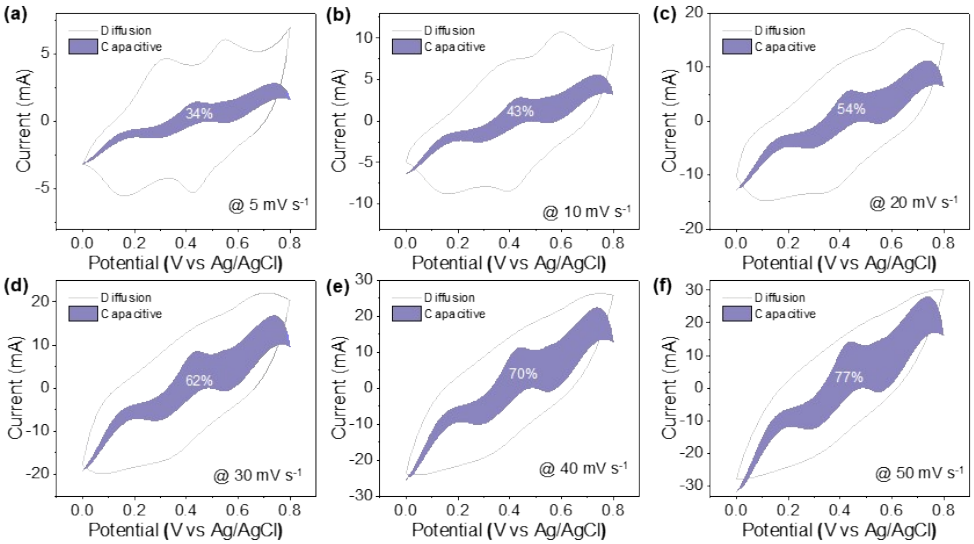

Fig. S44. Capacitive-controlled contribution of PTPAH@rGO3 film at different scan rates of (a) 5 mV s^{-1} , (b) 10 mV s^{-1}, (c) 20 mV s^{-1}, (d) 30 mV s^{-1}, (e) 40 mV s^{-1}, (f) 50 mV s^{-1} in a three-electrode system.

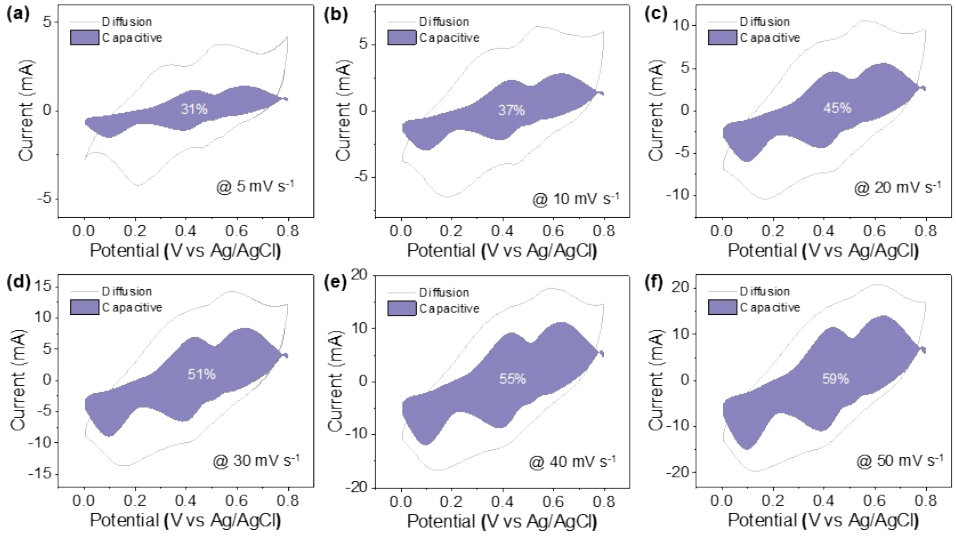

Fig. S45. Capacitive-controlled contribution of PTPAH@rGO1 film at different scan rates of (a) 5 mV s^{-1} , (b) 10 mV s^{-1}, (c) 20 mV s^{-1}, (d) 30 mV s^{-1}, (e) 40 mV s^{-1}, (f) 50 mV s^{-1} in a three-electrode system.

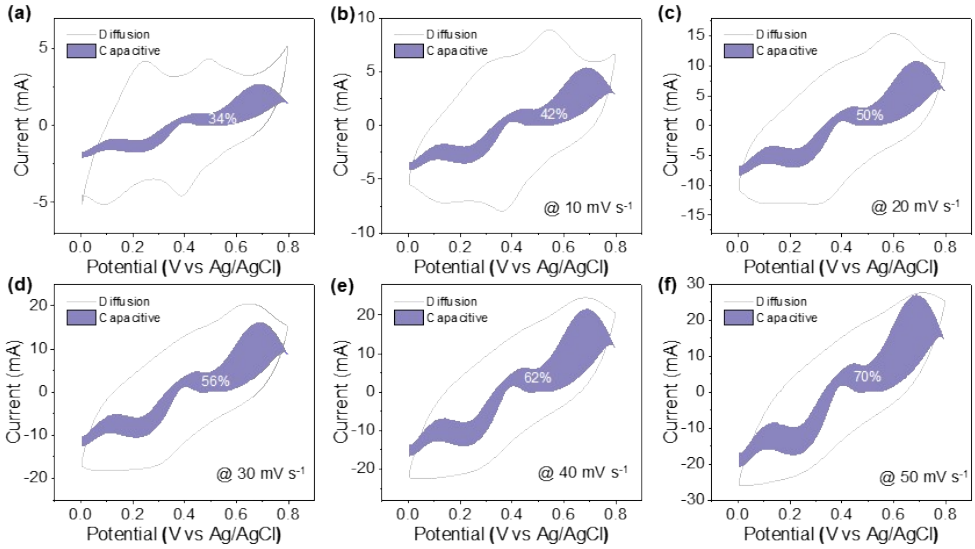

Fig. S46. Capacitive-controlled contribution of PTPAH@rGO2 film at different scan rates of (a) 5 mV s^{-1} , (b) 10 mV s^{-1}, (c) 20 mV s^{-1}, (d) 30 mV s^{-1}, (e) 40 mV s^{-1}, (f) 50 mV s^{-1} in a three-electrode system.

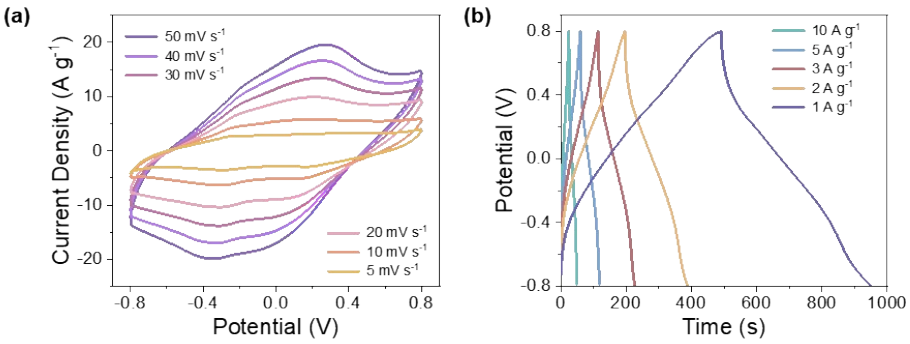

Fig. S47. (a) CV and (b) GCD curves of PTPAH@rGO1 film in a three-electrode system.

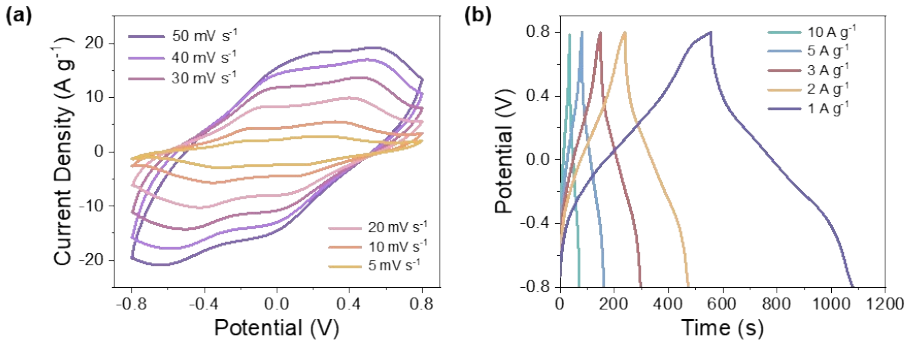

Fig. S48. (a) CV and (b) GCD curves of PTPAH@rGO2 film in a three-electrode system.

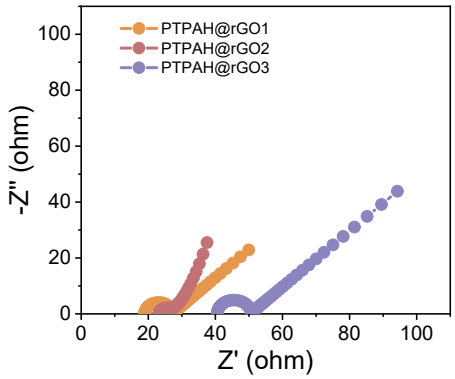

Fig. S49. Nyquist plot fitted with the R(C(RW))(C(RW)) equivalent of PTPAH@rGOs films in a two-electrode system.

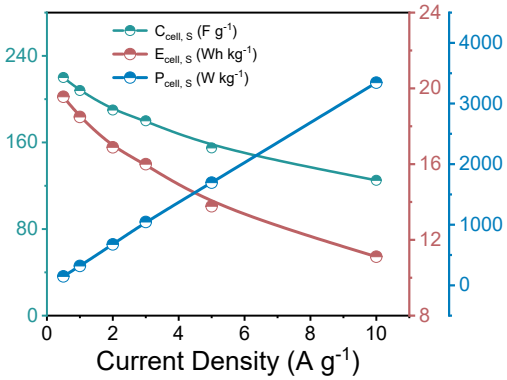

Fig. S50. The $C_{cell, S}$, $E_{cell, S}$, $P_{cell, S}$ of PTPAH@rGO2 FSSCs calculated based on GCD curves.

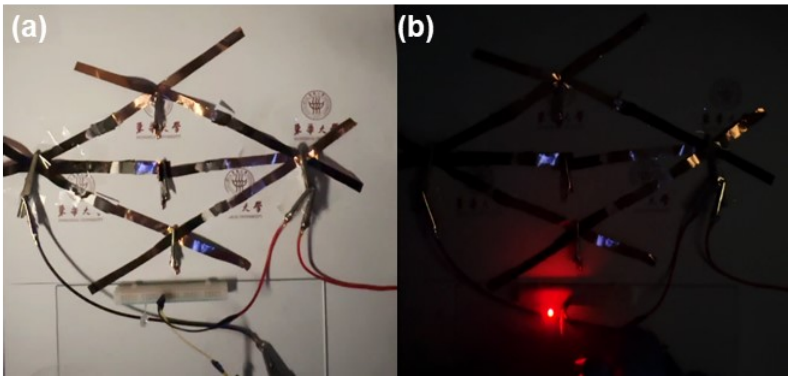

Fig. S51. (a-b) Photo images of the PTPAH@rGO2 FSSCs powering a red LED.

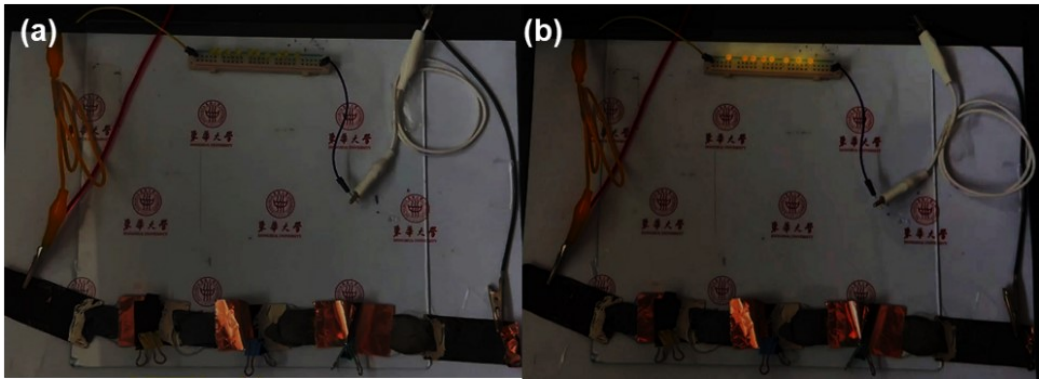

Fig. S52. (a-b) Photo images of the PTPAH@rGO2 FSSCs powering a row of yellow LEDs.

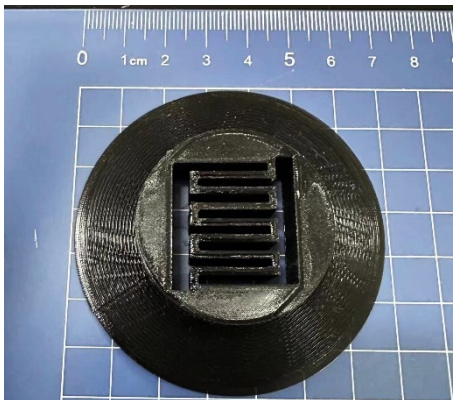

Fig. S53. Template prepared by 3D printing to prepare the interdigital electrode.

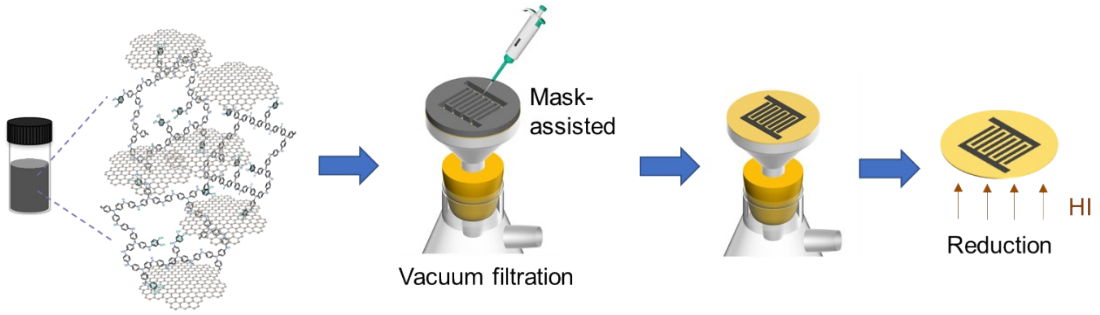

Fig. S54. Procedures for the preparation of PTPAH@rGOs film via an interdigital structure through mask-assisted method.

S4.2. Tables

Table S1. CMPs synthesized in different reaction solvents and their BET specific surface areas and yields. The samples synthesized in THF exhibited a higher specific surface area through BXJ approach.[7]

Sample	Solvent	BET surface area / m^2 g^{-1}	Yield
PTPA	Toluene	694	67%
PTPAH1	Toluene	643	64%
PTPAH2	Toluene	755	61%
PTPAH3	Toluene	704	57%
PTPAH4	Toluene	746	56%
PTPAH5	Toluene	740	51%
PTPA	THF	982	68%
PTPAH1	THF	890	65%
PTPAH2	THF	854	60%
PTPAH3	THF	1021	58%
PTPAH4	THF	1026	55%
PTPAH5	THF	986	51%

Table S2. The pore-structural parameters of CMPs synthesized in THF solvent.

Sample	V_{total} / cm^3 g^{-1}	V_{micro} / cm^3 g^{-1}	V_{micro} / V_{total}
PTPA	1.018	0.162	15.9%
PTPAH1	0.986	0.141	14.3%
PTPAH2	0.987	0.119	12.1%
PTPAH3	1.131	0.149	13.2%
PTPAH4	1.224	0.171	13.9%
PTPAH5	1.204	0.156	12.9%

Pore volume calculated from nitrogen adsorption at P/P_0 =0.95.

Micropore volume calculated from t-plot method

Table S3. The average resistance, resistivity and conductivity of rGO and PTPAH@rGO films measured through four-probe method.

Sample	Average resistance[a] / Ω	Average resistivity[a] ρ / Ω cm	Average conductivity[a] σ/ S m^{-1}
rGO	2.19	1.09×10^{-2}	8.81×10^{3}
PTPAH@rGO 1	4.3	3.26×10^{-2}	3.08×10^{3}
PTPAH@rGO 2	5.34	6.71×10^{-2}	1.49×10^{3}
PTPAH@rGO 3	9.15	1.16×10^{-1}	8.6×10^{2}

[a]The average resistance, resistivity, and conductivity are calculated based on three measured structures.

Table S4. The content ratio of characteristic peaks derived from C 1s XPS spectra of PTPAH@GOs/rGOs films.

Sample	The content ratio of characteristic peak				
	C=C/C-C (284.4 eV)	C-N (285.2 eV)	C-O (285.9 eV)	C=N (286.7 eV)	O-C=O (288.1-288.7 eV)
PTPAH@GO1	33%	15%	34%	12%	6%
PTPAH@GO2	24%	23%	28%	18%	7%
PTPAH@GO3	25%	20%	27%	22%	6%
PTPAH@rGO1	60%	15%	12%	10%	3%
PTPAH@rGO2	60%	13%	10%	13%	4%
PTPAH@rGO3	61%	14%	7%	14%	4%

Table S5. The area of characteristic peak for N 1s of PTPAH@rGOs.

Sample	Content ratio of peak (=N-) /peak (-NH-)
PTPAH@rGO1	44%
PTPAH@rGO2	56%
PTPAH@rGO3	51%
PTPAH3	42%

Table S6. Comparison of the electrochemical performance of PTPAH@rGOs electrodes with other

.

Sample	C_S / F g^{-1} (1 A g^{-1})	C_S (5 A g^{-1})/ C_S (1 A g^{-1})	C_S (10 A g^{-1})/ C_S (1 A g^{-1})	Ref.
PTPAH@rGO3	545	93.6%	82.6%	**This work**
LrGO	141 (1.04 A g^{-1})	85.8% (5.2 A g^{-1})	85.1% (11.4 A g^{-1})	[8]
Zn-mTCPP	142	/	/	[9]
CoNCCs	195	28.2%	25.6%	[10]
CoPc-CMP@CNTs	290	50.7%	41.7%	[11]
Mxene@rGO	337	85.4%	77.7%	[12]
COF@rGO	378	/	86.2%	[13]
PANI@rGO	407	/	93.3%	[14]
CMP-BT@CNT	477	84.1%	78.6%	[15]
PANI@CNT	500	70%	/	[16]
PANI@rGO-1L	536 (0.3 mA cm^{-2})	70% (1 mA cm^{-2})	/	[17]
PANI@SWCNT	541 (20 mv s^{-1})	/	/	[18]

Table S7. The calculated gravimetric, areal, volumetric capacitances for all samples.

Sample	System	C_G(F g^{-1})	C_A(mF cm^{-2})	C_V(F cm^{-3})
PTPAH@rGO1	Three-electrode	545	654	451
PTPAH@rGO2		420	504	202
PTPAH@rGO3		413	496	211
PTPAH@rGO1	Two-electrode	570	684	221
PTPAH@rGO2		564	677	271
PTPAH@rGO3		460	552	502
PTPAH@rGO2 FSSC	FSSC	220	264	106

Table S8. Comparison of the electrochemical performance of PTPAH@rGO2 FSSCs with previously-reported FSSCs.

Sample	Energy Density (Wh kg^{-1})	Power Density (W kg^{-1})	Ref.
PTPAH@rGO2	18.5	3344	**This work**
Mxene@rGO	19.7	750	[12]
PANI@rGO-1L	9	1100	[17]
PANI@SWCNT	7.2	1794	[18]
PANI@CNT@rGO	19.5	540	[19]
rGO	24	500	[20]
MV2//MnO2 ASC	20.8	375	[21]
porous MXene//Carbon Dots	17	1200	[22]
PCCN-K700	2.5	2500	[23]
PANI@BP	1.11	5000	[24]
PANS-co-oAP	4	1500	[25]
MWCNT@SACMP-3 SSC	9.5	3200	[26]

Table S9. Comparison of the electrochemical performance of PTPAH@rGO2 MSCs with previously reported conjugated polymer based and COF based MSCs.

Sample	$C_{cell, A}$ / mF cm^{-2}	Ref.
PTPAH@rGO2	54.6 (0.1 mA cm^{-2}), 28.6 (0.5 mA cm^{-2})	**This work**
PANI	13 (1 mA cm^{-2})	[27]
PANI	33 (0.4 mA cm^{-2})	[28]
5B-LIG	16.5 (0.05 mA cm^{-2})	[29]
COF@CNT	44.3 (5 mV s^{-1})	[6]
COF@rGO	26 (0.5 mA cm^{-2})	[30]

S5. Supplementary references

1. W. Lyu, W. Zhang, H. Liu, Y. Liu, H. Zuo, C. Yan, C. Faul, A. Thomas, M. Zhu and Y. Liao, *Chem. Mater.*, 2020, **32**, 8276-8285.
2. J. Zhang and X. Zhao, *ChemSusChem*, 2012, **5**, 818-841.
3. J. Huang, Y. Hu, J. Li, H. Wang, T. Wang, H. Wu, Y. Li, M. Wang and J. Zhang, *ACS Energy Lett.*, 2023, **8**, 2316-2324.
4. J. Wang, J. Polleux, J. Lim and B. Dunn, *J. Phys. Chem. C*, 2007, **111**, 14925-14931.
5. X. Wang, F. Huang, F. Rong, P. He, R. Que and S. P. Jiang, *J. Mater. Chem. A*, 2019, **7**, 12018-12028.

6. F. Zhang, S. Wei, W. Wei, J. Zou, G. Gu, D. Wu, S. Bi and F. Zhang, *Sci. Bull.*, 2020, **65**, 1659-1666.
7. J. Chen, W. Yan, E. J. Townsend, J. T. Feng, L. Pan, V. D. Hernandez and C. F. J. Faul, *Angew. Chem. Int. Ed.*, 2019, **58**, 11715-11719.
8. D. Yang and C. Bock, *J. Power Sources*, 2017, **337**, 73-81.
9. H. Zhang, Y. Zhang, C. Gu and Y. Ma, *Adv. Energy Mater.*, 2015, **5**, 1402175.
10. L. Mei, X. Cui, J. C. Wei, Q. Duan and Y. H. Li, *Dyes Pigm.*, 2021, **190**, 109299.
11. L. Mei, X. Cui, Q. Duan, Y. Li, X. Lv and H.-g. Wang, *International Int. J. Hydrog. Energy*, 2020, **45**, 22950-22958.
12. Y. Wang, N. Chen, Y. Liu, X. Zhou, B. Pu, Y. Qing, M. Zhang, X. Jiang, J. Huang, Q. Tang, B. Zhou and W. Yang, *Chem. Eng. J.*, 2022, **450**, 138398.
13. N. An, Z. Guo, J. Xin, Y. He, K. Xie, D. Sun, X. Dong and Z. Hu, *J. Mater. Chem. A*, 2021, **9**, 16824-16833.
14. Z. Xiong, Y. Cao, W.-J. Jiang, L. Zu, Q. Liang and D. Li, *Energy Stor. Mater.*, 2022, **53**, 444-452.
15. D. Roh, H. Shin, H. Kim and T. Kwon, *ACS Appl. Mater. Interfaces*, 2021, **13**, 61598-61609.
16. Y. Jiang, J. Ou, Z. Luo, Y. Chen, Z. Wu, H. Wu, X. Fu, S. Luo and Y. Huang, *Small*, 2022, **18**, 2201377.
17. H. Habib, I. S. Wani and S. Husain, *J Energy Storage*, 2022, **55**, 105732.
18. I. Panasenko, M. Bulavskiy, A. Iurchenkova, Y. Aguilar-Martinez, F. Fedorov, E. Fedorovskaya, B. Mikladal, T. Kallio and A. Nasibulin, *J. Power Sources*, 2022, **541**, 231691.
19. D. Wu, C. Yu and W. Zhong, *J. Mater. Chem. A*, 2021, **9**, 18356-18368.
20. G. Lian, C. Tuan, L. Li, S. Jiao, K. Moon, Q. Wang, D. Cui and C. Wong, *Nano Lett.*, 2017, **17**, 1365-1370.
21. W. Luo, Y. Sun, Z. Lin, X. Li, Y. Han, J. Ding, T. Li, C. Hou and Y. Ma, *J Energy Storage*, 2023, **62**, 106807.
22. Y. Wang, N. Chen, B. Zhou, X. Zhou, B. Pu, J. Bai, Q. Tang, Y. Liu and W. Yang, *Nanomicro Lett*, 2023, **15**, 231.
23. T. Feng and G. Liu, *J Energy Storage*, 2023, **74**, 109489.
24. J. Vaghasiya, K. Kripalova, S. Hermanova, C. Mayorga-Martinez and M. Pumera, *Small*, 2021, **17**, 2102337.
25. C. Wang, Y. Yang, Z. Zhou, Y. Li, Y. Li, W. Hou, S. Liu and Y. Tian, *Small*, 2023, **20**, 2305994.
26. W. Lyu, C. Yan, Z. Chen, J. Chen, H. Zuo, L. Teng, H. Liu, L. Wang and Y. Liao, *ACS Appl. Energy Mater.*, 2022, **5**, 3706-3714.
27. M. Yang, Y. Liu, X. Luo, Y. Cao, X. Gong and W. Xu, *ACS Appl. Energy Mater.*, 2021, **4**, 10069-10080.
28. L. Li, Z. Lou, W. Han, D. Chen, K. Jiang and G. Shen, *Adv. Mater. Technol.*, 2017, **2**, 1600282.
29. Z. Peng, R. Ye, J. Mann, D. Zakhidov, Y. Li, P. Smalley, J. Lin and J. Tour, *Acs Nano*, 2015, **9**, 6, 5868-5875.
30. M. Yao, C. Guo, Q. Geng, Y. Zhang, X. Zhao, X. Zhao and Y. Wang, *Ind. Eng. Chem. Res.*, 2022, **61**, 7480-7488.